

Computer Methods in Applied Mechanics and Engineering

Enhanced Material Point Method to face dynamic problems: Local-maximum entropy approximation and explicit predictor-corrector scheme

Miguel Molinos^a Pedro Navas^{a1}, Manuel Pastor^a and Miguel Martn Stickle^a

^a *ETSI Caminos, Canales y Puertos, Universidad Politécnica de Madrid.
c. Prof. Aranguren 3, 28040 Madrid, Spain*

Abstract

Material Point Method (MPM) has arisen in the recent years as an alternative to Finite Element Method (FEM) under the large deformation regime. However, the simulation of shock waves propagation and other high frequency problems is still challenging under this approach due the incapability of the standard MPM time integration scheme to filter spurious noises. To overcome this limitation in this paper, an explicit predictor-corrector time integration scheme has been proposed. Its superior performance mitigates the presence of spurious oscillations with minimal dissipation in high frequency problems. Other source of numerical noise in MPM occurs when to material points cross computational grid boundaries and motivated due to the lack of smoothness of the interpolation functions. This noise results in spurious local variations at the material points, where strain-stress fields are computed. This could invalidate the solution in one case, or damage it in another. To overcome it, this document adopts the Local Maximum-Entropy (LME) approximation schemes a robust substitute for the wide range of shape function in MPM. LME approximation may be regarded as a *thermalization* of Delaunay triangulation which resolves the degenerate cases resulting from the lack or uniqueness of the triangulation. Furthermore, by modifying a regularization parameter they are able to behave finite element like or as a mesh-free method. This capability allows to face a wide range of physics with a single shape function family. Finally this paper demonstrates the performance of both improvements thorough numerical examples.

Keywords: LME, MPM, Explicit predictor-corrector, Dynamic problems

¹Corresponding author: p.navas@upm.es

1. Introduction

Since the proposal of MPM by Sulsky *et al.* (1994) [1] as a generalization to solids of the Fluid Implicit Particle (FLIP) method [2]. Its popularity has increased due to its ability to deal with large strain regime without suffer
5 mesh distortion inaccuracies.

However, this method suffers other kind of instabilities, such those when material points crossing cell boundaries. This give rise to the development of other interpolation techniques to overcome this limitation such as the Generalized Interpolation Material Point (GIMP) method Bardenhagen & Kober
10 (2004) [3], which has demonstrate to have a good performance in the finite deformation regime. However, in the absence of a regular grid, construction of the weighting functions is only achieved at considerable effort and computational cost. Furthermore, as it is a voxel based discretization technique, it is prone to suffer voxel domains overlap or gaps when the material
15 point mesh becomes irregular, which can introduce severe inaccuracies as noticed Steffen *et al.* (2008)[4]. This is similar to the difficulty encountered by the finite element methods due to element distortion. A more robust alternative is the Dual Domain Material Point (DDMP) method proposed by Zhang *et al.* (2011) [5]. Unfortunately this method shows an unsatisfactory
20 behaviour when particle/cell ratio decreases [6], therefore DDMP requires a large number of particles needed for convergence, this makes the method very expensive. In recent years the employ of spline-lines has gain popularity with the introduction of the B-Spline MPM proposed by Roel Tielen *et al.* (2017) [7], this technique allows the employ of unstructured set of nodes
25 and particles. More recently, approximants derived from minimization has been introduced in to MPM framework with the Conservative Taylor Least Squares (CTLS) reconstruction proposed by Wobbes *et al.* (2018) [8], unfortunately when particles are spread in a challenging way, the quality of the CTLS approximation decrease locally.

30 This document adopts the LME or local *max-ent* as a robust substitute for the wide range of shape function in MPM. First introduced by Arroyo & Ortiz (2006) [9], it belongs to the class of convex approximation schemes and provides a seamless transition between FEM and mesh-free interpolations. The approximation scheme is based on a compromise between minimizing
35 the width of the shape function support and maximizing the information entropy of the approximation. The local *max-ent* approximation may be regarded as a regularization, or *thermalization*, of Delaunay triangulation which effectively resolves the degenerate cases resulting from the lack of uniqueness or the triangulation. Local *max-ent* basis functions possess many desirable
40 properties for mesh-free algorithms. First of all, they are entirely defined

by the nodal set and the domain of analysis. They are also non-negative, satisfy the partition of unity property, and provide an exact approximation for affine functions [9]. This approximation scheme has been proof to have a good performance under the dynamic regime by other researchers like Navas
45 *et al.* (2018) [10] and Li *et al.* (2012) [11] for Optimal Transportation Mesh-free (OTM) method. And more recently under MPM framework by Wobbes
et al.(2020) [12] but without exploring the benefits of the regularization parameter β .

This techniques are devoted to mitigate the “grid crossing” error. Nevertheless, in the presence of shock waves spurious numerical noises appears
50 despite of this using techniques [13]. These numerical inaccuracies also known as wiggles are due to inaccuracies in the time discretization technique. A simple approach to face those spurious noises is to add a nonphysical damping source to the equilibrium equations, this approach has been widely employed
55 in this and many other numerical techniques. To avoid introducing this non-physical sources, many researchers has proposed alternative time integration schemes which reduce the presence of high frequency noises by filtering them or increasing the accuracy of the time integration scheme. One of the most popular is the Implicit GIMP (iGIMP) Charlton *et al.* (2017) [14], more
60 recently Tran & Solowski (2019) [13] proposed a generalised- α scheme for MPM with promising results but at the expense of increasing the computational effort. In this paper a less time consuming and high efficient explicit predictor corrector integration method has been proposed. It consists in an accommodation of the npc. This method has been chosen among other suitable
65 alternatives as those proposed by Wilson *et al.* (1972) [15] or Chung & Hulbert (1993) [16] because it simplicity and it good performance dealing with solids dynamics problems under a mesh-free framework in [10].

The aim of this document is to mitigate the spurious oscillations due inaccuracies in both space and time discretization by the employ of a suitable
70 combination of the LME family shape functions, and the proposal of a explicit predictor-corrector scheme. The advantages of this approach will be illustrated thorough to simple but challenging test cases, like the propagation of shock waves in a elastic bar or the response of a block of soil gradually loaded with gravitational forces.

The article is organized as follows. Section 2 is devoted to describe the
75 meshfree methodology adopted in this research, first MPM procedure is introduced in 2.1, second the explicit predictor-corrector time integration scheme is presented in 2.2, and third LME approximation scheme will be introduced in 2.3. In Section 3 applications to prove the numerical accuracy of the proposed approach are presented. Finally, conclusions and future research topics
80 are exposed in Section 4.

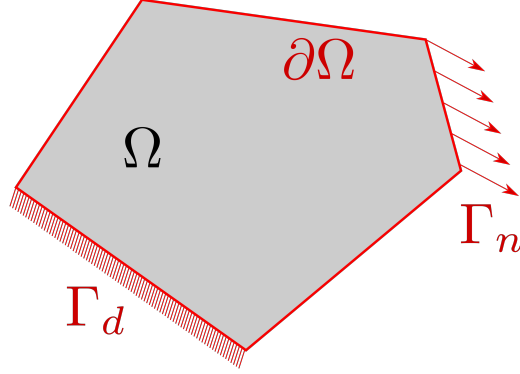


Figure 1: Description of the boundary-value-problem in a continuum. Red lines represents the closure $\partial\Omega$ of the domain Ω represented in gray.

2. The meshfree methodology

The aim of this section is to provide an overview of the standard explicit MPM algorithm [1]. Without losing generality, the method has three main steps: (i) a variational recovery process, where particle data is projected to the grid nodes, (ii) an Eulerian step, where balance of momentum equation is expressed as a nodal equilibrium equation thorough a FEM-like procedure, and finally (iii) a Lagrangian advection of the particles. In consequence MPM can be regarded as a Lagrangian-Eulerian method where particles carries on all the physical information and a set of background nodes is employed to compute the equilibrium equation. In what follows, we will adopt the following convention. Three kind of subscript or superscript are used within paper. The subscript \square_p is used to define a particle variable. While the subscript \square_I is reserved in this notation for denoting nodal variables. And finally, the superscript \square^ψ involves a virtual magnitude. For the operators, the convention is : $\dot{\square}$ and $\ddot{\square}$ for the first and second time derivative, \otimes means the dyadic operator, $\square \cdot \square$ and $\square : \square$ means the first and second contraction of a tensor, $div(\square)$ denotes the divergence operator, and finally $grad(\square)$ and $grad^s(\square)$ denotes the gradient and its symmetric part. Einstein subscripts convention is adopted therefore repeated index means addition.

2.1. Derivation of MPM procedure

In MPM the continuum mechanics approach is considered. So on, let define a continuum Ω occupied by an elastic body like the sketched in the figure 1, and $\partial\Omega$ the boundaries of the domain defined by $\partial\Omega = \Gamma_d \cup \Gamma_n$ and $\Gamma_d \cap \Gamma_n = \emptyset$. In this context the field u allows to describe the *global state* of the system. Now the variable $\phi = (\varepsilon, \sigma)$ is defined as the set of *local states* at any point of the continuum which can be derived from the field u through the

following set of governing equations and restrictions that must be satisfied. First (i) the *compatibility equation* that extracts from u the strain field ε is,

$$\varepsilon = \text{grad}^s(u), \quad (1)$$

together with essential boundary conditions of Dirichlet type Γ_d . An additional consideration over the strain field is the assumption of infinitesimal strain, therefore second order terms in the spatial derivatives can be neglected. The corresponding conjugate variable for the strain field is the stress field σ , which satisfies (ii) the *conservation of momentum equation*

$$\rho \frac{Dv}{Dt} = \text{div}(\sigma) + \rho b \quad (2)$$

together with the natural boundary conditions of the Neumann type Γ_n . Next (iii) the constitutive equation as a linear application from \mathfrak{R}^n to \mathfrak{R}^n , which relates the strain tensor with the stress tensor,

$$\sigma = \mathbf{D} : \varepsilon. \quad (3)$$

The final restriction is (iv) the mass conservation, which can be obtained by setting to zero the total derivative of the density field,

$$\frac{D\rho}{Dt} = \dot{\rho} + \rho \text{div}(v) = 0. \quad (4)$$

To write the variational statement of the problem, let us define a virtual displacement field such that

$$u^\psi \in \mathcal{H}_0^1(\Omega) = \{u^\psi \in \mathcal{H}^1 \mid u^\psi = 0 \text{ on } \Gamma_d\}. \quad (5)$$

And which satisfies that the Cauchy sequences are convergent in Ω

$$\int_{\Omega} u^\psi \, d\Omega < \infty \quad \text{and} \quad \int_{\Omega} \varepsilon^\psi \, d\Omega < \infty \quad (6)$$

The principle of virtual work states that the equilibrium solution to the boundary-value problem of elasticity is the function $u \in \mathcal{H}_0^1$ such that, for $u^\psi \in \mathcal{H}_0^1$, the following holds:

$$\int_{\Omega} \rho \left(\frac{d\vec{v}}{dt} - \vec{b} \right) \cdot \vec{u}^\psi \, d\Omega = \int_{\Gamma_d} \vec{t} \cdot \vec{u}^\psi \, d\Gamma - \int_{\Omega} \sigma : \varepsilon^\psi \, d\Omega, \quad (7)$$

therefore (7) together with (3) and (4) represents the weak form formulation of the problem.

105 In order to arrive to a finite set of equations, in contrast with the FEM,
in MPM a double discretization procedure is performed. First, the contin-
uum Ω is discretized with a finite sum of material points (in the following
particles), each one represent a part of the discretized domain $\Omega_p \subset \Omega$ with
 $p = 1, 2 \dots, N_p$ where N_p is the number of particles. The material point \vec{x}_p is
110 defined at the centroid of each Ω_p , figure 2. Each material point is assigned
with initial values of position, velocity, mass, volume and stress denoted by
 $\vec{x}_p, \vec{v}_p, m_p, V_p$ and σ_p , but also the virtual displacement field u_p^ψ . Therefore,
employing the definition of the material integral, where Riemann integral
definition is recovered as an addition of a finite set of points, and their vol-
115 umes are interpreted as quadrature weights. Consequently, individual terms
in (7) are solved as follows.

- Acceleration forces :

$$\int_{\Omega} \rho \frac{d\vec{v}}{dt} \cdot u^\psi d\Omega = \frac{d\vec{v}_p}{dt} \cdot u_p^\psi m_p. \quad (8)$$

- Internal forces :

$$\int_{\Omega} \sigma : \varepsilon^\psi d\Omega = \sigma_p : \varepsilon_p^\psi V_p. \quad (9)$$

120

- Body forces :

$$\int_{\Omega} \rho \vec{b} \cdot u^\psi d\Omega = \vec{b}_p \cdot u_p^\psi m_p. \quad (10)$$

- Loads :

$$\int_{\Gamma_d} \vec{t} u^\psi d\Gamma = \int_{\Gamma_d} \rho \vec{t}^\sharp \cdot u^\psi d\Gamma = \vec{t}_p^\sharp \cdot u_p^\psi h^{-1} m_p, \quad (11)$$

where h is the thickness of the continuum in a 2D case. Here is where the
second discretization procedure appears. A background mesh composed by
a finite set of grid points with coordinates $\vec{x}_I, I = 1, 2 \dots, N_n$, is generated.
Where N_n is the number of grid nodes. This mesh is employed as a support
to compute gradients and divergences. Introducing (8), (9), (10), (11) in (7),
approximating the displacement field of the particle p as $\vec{u}_p = N_{Ip} u_I, \vec{u}_p^\psi =$

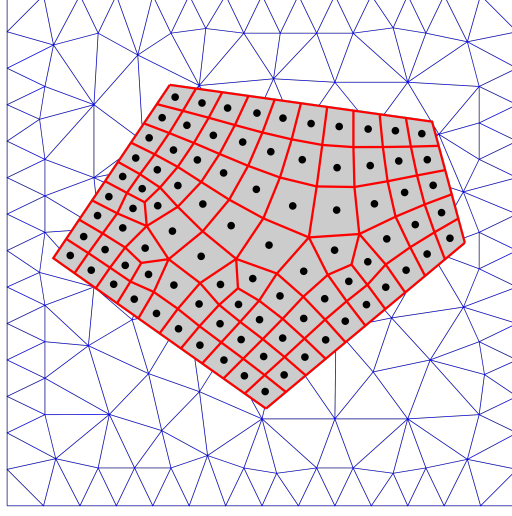


Figure 2: Description of the spatial discretization for domain presented in the figure 1. Blue mesh represent the background computational support, and the grid mesh conforms the discretized continuum body.

$N_{Ip}u_I^\psi$, and its gradient as $\varepsilon_p = (u_I \otimes \text{grad}(N_{Ip}))^s$, $\varepsilon_p^\psi = (u_I^\psi \otimes \text{grad}(N_{Ip}))^s$. nodal balance of forces of the continuum is obtained,

$$\dot{\vec{p}}_I = \mathbf{m}_{IJ}\dot{\vec{v}}_J = \vec{f}_I^{int} + \vec{f}_I^{ext}, \quad (12)$$

where $\dot{\vec{p}}_I$ is the rate of momentum at grid node I , the nodal mass matrix \mathbf{m}_{IJ} is,

$$\mathbf{m}_{IJ} = N_{Ip}m_pN_{Jp}. \quad (13)$$

To improve the computational efficiency and stability, the nodal mass matrix (13) can be substituted by the lumped mass matrix \mathbf{m}_{IJ}^{lumped} . Later, internal and external forces are computed as follows,

$$\vec{f}_I^{int} = -\sigma_p \cdot \text{grad}(N_{Ip}) \frac{m_p}{\rho_p} \quad (14)$$

$$\vec{f}_I^{ext} = N_{Ip} \vec{b}_p m_p + N_{Ip} \vec{t}_p^s m_p h^{-1} \quad (15)$$

where $\sigma_p = \sigma_p(\varepsilon_p)$ is the particle p stress field, which can be integrated employing the suitable constitutive model. The strain tensor is updated employing the rate of stress tensor $\dot{\varepsilon}_p$ used to update the strain tensor is as follows (16).

$$\dot{\varepsilon}_p = \frac{\Delta \varepsilon_p}{\Delta t} = \frac{1}{2} [\text{grad}(N_{Ip}) \otimes \vec{v}_I + \vec{v}_I \otimes \text{grad}(N_{Ip})]. \quad (16)$$

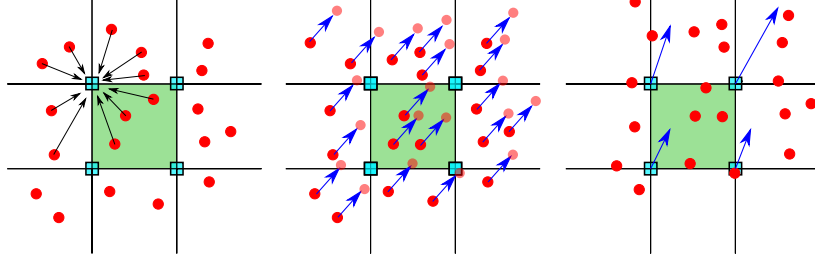


Figure 3: Description of the three steps in MPM standard algorithm.

Next, mass conservation is guaranteed by enforcing the null value of the material derivative of the density field $\frac{D\rho}{Dt} = 0$. This leads a suitable equation to update the density field.

$$\dot{\rho} = -\rho \text{ trace } (\dot{\epsilon}) \quad (17)$$

Finally, to solve the equation (12), a second order temporal integration scheme is required. Therefore, time is discretized in to a finite set of time steps $k = 1 \dots, Nt$, where k is the current time step and Nt is the total number of time steps. Once the nodal equilibrium equation it is solved, the values in the nodes are interpolated back in to the particles and each particle it is advected to the new position,

$$\dot{\vec{v}}_p = N_{Ip} \vec{a}_I, \quad \text{and} \quad \dot{\vec{x}}_p = N_{Ip} \vec{v}_I \quad (18)$$

In MPM literature, this equations (12) and (18), is solved with an explicit forward Euler algorithm. The time integration scheme of MPM has been described in detail by many researchers [1], [17], [18] and summarized in figure 3. Other authors have proposed many others time integration alternatives like [19], [13], [14]. In the first publication on MPM [1], the nodal acceleration was employed to update the particles as

$$v_p^{k+1} = v_p^k + \Delta t N_{Ip}^k \vec{a}_I^k \quad (19)$$

$$x_p^{k+1} = x_p^k + \Delta t N_{Ip}^k \vec{v}_I^k. \quad (20)$$

However, as Andersen (2009)[18] point out, this algorithm has been shown to be numerically unstable due to that $f_I^{int,k}$ can be finite for an infinitesimal nodal mass \mathbf{m} . This can lead to numerical issues when nodal acceleration is obtained for evaluating (20),(19). Hence, a corrected version of this algorithm in shown in Zhang *et al.* (2016)[20]

$$x_p^{k+1} = x_p^k + \Delta t \frac{N_{Ip}^k \vec{p}_I^k}{\mathbf{m}_I}. \quad (21)$$

$$v_p^{k+1} = v_p^k + \Delta t \frac{N_{Ip}^k \vec{f}_I^k}{\mathbf{m}_I}, \quad (22)$$

Later Tran & Solowski (2019)[13] presented a generalized- α scheme for MPM inspired in the explicit time integration algorithm proposed by Chung & Hulbert (1993)[16], but with the particularity that the acceleration is evaluated both in the beginning and the end of the time step.

$$v_p^{k+1} = v_p^k + \Delta t N_{Ip}^k [(1 - \gamma) a_I^k + \gamma a_I^{k+1}], \quad (23)$$

$$x_p^{k+1} = x_p^k + N_{Ip}^k \left[\Delta t \vec{v}_I^k + \Delta t^2 \left(\left(\frac{1}{2} - \beta \right) \vec{a}_I^k + \beta \vec{a}_I^{k+1} \right) \right] \quad (24)$$

$$a_p^{k+1} = N_{Ip}^k \vec{a}_I^{k+1}. \quad (25)$$

125 This scheme has proof to damps out the higher frequency noises [13]. But it can present the same numerical instabilities as in (20),(19) when nodal masses become infinitesimal, and requires extra storage for nodal values of acceleration and previous steps.

2.2. Explicit predictor-corrector scheme for MPM.

In this section, a explicit predictor-corrector time integration scheme is presented. It is based in the Newmark a-form $\gamma = 0.5$ and $\beta = 0$ which is the central difference explicit. This method is devoted to solve a system of equations of the type

$$\mathbf{M}_{IJ} \ddot{\mathbf{d}}_J + \mathbf{C}_{IJ} \dot{\mathbf{d}}_J + \mathbf{K}_{IJ} \mathbf{d}_J = \mathbf{F}_I.$$

As MPM has a nodal stage, it is possible to apply this methods successfully in MPM framework as were proved by [13]. Taking the predictor definition from and calculating nodal velocities, and updating particles position employing nodal values of velocity and acceleration. The predictor-corrector algorithm has been described in the classic literature [21], and its computational advantages and stability were widely proof by Liu [22]. The “classic” Newmark Predictor-Corrector (NPC) algorithm starts with a predicted value of the nodal velocities at the $(k + 1)$ th time step denoted by \vec{v}_I^{k+1} given as,

$$\vec{v}_I^{k+1} = \vec{v}_I^k + (1 - \gamma) \Delta t \vec{a}_I^k \quad (26)$$

In (26) arise a *user-defined* parameter $\gamma \geq 0$. This parameter influences both the predictor accuracy and the stability of the algorithm. As point out Liu

¹³⁰ [22], the truncation error of the predictor formula is $O(\Delta t^3)$ when $\gamma = 0.5$, and is unconditionally stable if $0 < \gamma \leq 0.25$.

To accommodate this step to MPM framework, it is necessary to get the nodal values of the velocity and acceleration throughout a variational recovery process where particles quantities are transferred to the mesh nodes. This technique arise as a generalization of the super-convergent recovery procedures described by Zienkiewicz & Zhu [23] (ZZ) in the context of FEM. In MPM Gauss quadrature is not employed as integrals are computed following the Riemann integral definition, where each component of the summation correspond to a particle of the discretization. Also Bardenhagen & Kober [3] proved that thorough this information-transference technique mass and momentum are conserved. So for a general particle variable Φ_p employing the ZZ technique is possible to get its nodal homologous Φ_I as,

$$\Phi_I = \frac{m_p N_{Ip} \Phi_p}{m_I} \quad (27)$$

Therefore, to get a analogous expression for (26) in the context of MPM, the procedure described in the equation (27) is employed reaching to,

$$\vec{v}_I^{k+1} = \underbrace{\frac{N_{Ip}^k m_p \vec{v}_p^k}{m_I}}_{\vec{v}_I^k} + (1 - \gamma) \Delta t \underbrace{\frac{N_{Ip}^k m_p \vec{a}_p^k}{m_I}}_{\vec{a}_I^k} \quad (28)$$

Nonetheless this way of computing the predictor stage can introduce instabilities due to numerical cancellation likewise the original Sulky algorithm. Thankfully this can be avoided easily by the equivalent formulation (29),

$$\vec{v}_I^{k+1} = \frac{N_{Ip}^k m_p (\vec{v}_p^k + (1 - \gamma) \Delta t \vec{a}_p^k)}{m_I} \quad (29)$$

This way of computing the nodal predictor is both numerically stable and minimize the computational effort. Once nodal velocities are obtained, the essential boundary conditions are imposed over Γ_d . And in the following, the “classic” MPM algorithm continues to reach to the equilibrium equation (12). Now the *corrector* stage is introduced. Due to the fact that nodal velocities were obtained earlier, this step is computed in the same way as in FEM,

$$\vec{v}_I^{k+1} = \vec{v}_I^{pred} + \gamma \Delta t \frac{\vec{f}_I^{k+1}}{\mathbf{m}_I^{k+1}} \quad (30)$$

Finally updated particle kinetics are computed using nodal values as,

$$\vec{a}_p^{k+1} = \frac{N_{Ip}^k \vec{f}_I^k}{\mathbf{m}_I^k} \quad (31)$$

$$\vec{v}_p^{k+1} = \vec{v}_p^n + \Delta t \frac{N_{Ip}^k \vec{f}_I^k}{\mathbf{m}_I^k} \quad (32)$$

$$\vec{x}_p^{k+1} = \vec{x}_p^n + \Delta t N_{Ip}^k \vec{v}_I^k + \frac{1}{2} \Delta t^2 \frac{N_{Ip}^k \vec{f}_I^k}{\mathbf{m}_I^k} \quad (33)$$

Notice that particle displacement is computed using the corrected nodal velocities and the accelerations computed with the velocities of the predictor. However, particles velocities and accelerations are computed using the corrected velocities. Therefore here we share similarities with the *leapfrog integration* which updates the position at full time step, but updates the velocity at half time steps. Notice also that with this approach the calculation of nodal momentum values are not required. Due to its simplicity allows be implemented with minor modifications over a standard forward Euler. It is summarized in shape of pseudo-algorithm.

2.3. Local max-ent approximants

The popularity of MPM has increase notoriously during the recent years due to its ability to deal with large strain problems without mesh distortion issues inherent to mesh based methods like FEM, see Zdzislaw [24]. However, in the simulations made with the original MPM, there are numerical noises when particles crossing the cell boundaries. Local Maximum-Entropy (LME) approximation schemes were first introduced by Arroyo & Ortiz (2006)[9] has been recently tested under MPM framework by Wobbes *et al.* (2020)[12] where they prof that simulations performed with LME, shows considerably more accurate stress approximations for MPM. Although, in [12] authors does not deep in how the regularization parameter β affects to the accuracy and stability of the solution. The basic idea of the shape functions based on such an estimate is to interpret the shape function $N_I(\vec{x})$ as a probability. This allow us to introduce two important limits: the principle of maximum-entropy (*max-ent*) statistical inference stated by [25], and the Delaunay triangulation which ensures the minimal width of the shape function.

This approximation scheme represents a optimal compromise, in the sense of Pareto, between the *unbiased statistical inference* based on the nodal data which leads to the principle of *maximum-entropy* stated by Jaynes [25], and the definition of local shape functions of *least width* the least biased shape functions.

Algorithm Newmark Predictor-Corrector (NPC) scheme

1: **Update mass matrix:**

$$\mathbf{m}_I = N_{Ip}^k m_p,$$

2: **Explicit Newmark Predictor:**

$$\vec{v}_I^{pred} = \frac{N_{Ip}^k m_p (\vec{v}_p^k + (1 - \gamma) \Delta t \vec{a}_p^k)}{m_I}$$

3: **Impose essential boundary conditions:**

At the fixed boundary, set $\vec{v}_I^{pred} = 0$.

4: **Deformation tensor increment calculation.**

$$\begin{aligned} \dot{\varepsilon}_p^{k+1} &= \left[\vec{v}_I^{pred} \otimes \text{grad}(N_{Ip}^{k+1}) \right]^s \\ \Delta \varepsilon_p^{k+1} &= \Delta t \dot{\varepsilon}_p^{k+1} \end{aligned}$$

5: **Update the density field:**

$$\rho_p^{k+1} = \frac{\rho_p^k}{1 + \text{tra} [\Delta \varepsilon_p^{k+1}]}.$$

6: **Balance of forces calculation:**

Calculate the total grid nodal force $\vec{f}_I^{k+1} = \vec{f}_I^{int,k+1} + \vec{f}_I^{ext,k+1}$ evaluating (14) and (15) in the time step $k + 1$. In the grid node I is fixed in one of the spatial dimensions, set it to zero to make the grid nodal acceleration zero in that direction.

7: **Explicit Newmark Corrector:**

$$\vec{v}_I^{k+1} = \vec{v}_I^{pred} + \gamma \Delta t \frac{\vec{f}_I^{k+1}}{\mathbf{m}_I^{k+1}}$$

8: **Update particles lagrangian quantities:**

$$\begin{aligned} \vec{a}_p^{k+1} &= \frac{N_{Ip}^k \vec{f}_I^k}{\mathbf{m}_I^k} \\ \vec{v}_p^{k+1} &= \vec{v}_p^k + \Delta t \frac{N_{Ip}^k \vec{f}_I^k}{\mathbf{m}_I^k} \\ \vec{x}_p^{k+1} &= \vec{x}_p^k + \Delta t N_{Ip}^k \vec{v}_I^k + \frac{1}{2} \Delta t^2 \frac{N_{Ip}^k \vec{f}_I^k}{\mathbf{m}_I^k} \end{aligned}$$

9: **Reset nodal values**

Taking the definition of entropy as a measure of how uncertainty a random variable is averaged on all its possible outcomes. And adopting the Shannon's entropy as the starting point:

$$H(p_1(\vec{x}), \dots, p_n(\vec{x})) = - \sum_{I=1}^{N_n} p_I(\vec{x}) \log p_I \quad (34)$$

where $p_I(\vec{x})$ is the probability, equivalent to the mentioned shape function $N_I(\vec{x})$, satisfying both the zeroth and first-order consistency. The least-biased approximation scheme is given by

$$\begin{aligned} \text{(LME) Maximize } H(N_I) &\equiv - \sum_I^{N_n} N_I(\vec{x}) \log N_I \\ \text{subject to } &\begin{cases} N_I \geq 0, \text{ I}=1, \dots, n \\ \sum_{I=1}^{N_n} N_I = 1 \\ \sum_{I=1}^{N_n} N_I \vec{x}_I = \vec{x} \end{cases} \end{aligned}$$

On the other hand, the control of the shape function width and its decay with distance away from the corresponding nodes is a desirable property. To reach to this objective [9] propose the following linear program,

$$\begin{aligned} \text{(RAJ) For fixed } \vec{x} \text{ minimize } U(\vec{x}_p, N_I) &\equiv \sum_I N_I |\vec{x}_p - \vec{x}_I|^2 \\ \text{subject to } &\begin{cases} N_I \geq 0, \text{ I}=1, \dots, n \\ \sum_{I=1}^{N_n} N_I = 1 \\ \sum_{I=1}^{N_n} N_I \vec{x}_I = \vec{x} \end{cases} \end{aligned}$$

To reach to a compromise between two competing objectives, a Pareto set is

defined by [9] as,

$$\begin{aligned}
 &(\text{LME})_\beta \text{ For fixed } \vec{x} \text{ minimize } f_\beta(\vec{x}, N_I) \equiv \beta U(\vec{x}, N_I) - H(N_I) \\
 &\text{subject to } \begin{cases} N_I \geq 0, \text{ I}=1, \dots, n \\ \sum_{I=1}^{N_n} N_I = 1 \\ \sum_{I=1}^{N_n} N_I \vec{x}_I = \vec{x} \end{cases}
 \end{aligned}$$

The regularization o *thermalization* parameter between the two criterion β has Pareto optimal values in the range $\beta \in (0, \infty)$. The unique solution of the local *max-ent* problem LME_β is:

$$N_I^*(\vec{x}) = \frac{\exp \left[-\beta |\vec{x} - \vec{x}_I|^2 + \vec{\lambda}^* \cdot (\vec{x} - \vec{x}_I) \right]}{Z(\vec{x}, \vec{\lambda}^*)} \quad (35)$$

where

$$Z(\vec{x}, \vec{\lambda}) = \sum_{I=1}^{N_n} \exp \left[-\beta |\vec{x} - \vec{x}_I|^2 + \vec{\lambda} \cdot (\vec{x} - \vec{x}_I) \right] \quad (36)$$

being $\vec{\lambda}^*(\vec{x})$ the unique minimiser for the function $\log Z(\vec{x}, \vec{\lambda})$. The traditional way to obtain such a minimiser is using Eq. (37) to calculate small increments of $\partial \vec{\lambda}$ in a Newton-Raphson approach. Where \mathbf{J} is the Hessian matrix, defined by:

$$\mathbf{J}(\vec{x}, \vec{\lambda}, \beta) \equiv \frac{\partial \vec{r}}{\partial \vec{\lambda}} \quad (37)$$

$$\vec{r}(\vec{x}, \vec{\lambda}, \beta) \equiv \frac{\partial \log Z(\vec{x}, \vec{\lambda})}{\partial \vec{\lambda}} = \sum_I^{N_n} p_I(\vec{x}, \vec{\lambda}, \beta) (\vec{x} - \vec{x}_I) \quad (38)$$

In order to obtain the first derivatives of the shape function, it is also necessary to compute ∇N_I^*

$$\nabla N_I^* = N_I^* \left(\nabla f_I^* - \sum_J^{N_n} N_J^* \nabla f_J^* \right) \quad (39)$$

where

$$f_I^*(\vec{x}, \vec{\lambda}, \beta) = -\beta |\vec{x} - \vec{x}_I|^2 + \vec{\lambda} \cdot (\vec{x} - \vec{x}_I) \quad (40)$$

Employing the chain rule, rearranging and considering β as a constant, Arroyo and Ortiz [9] obtained the following expression for the gradient of the sahep function.

$$\nabla N_I^* = -N_I^* (\mathbf{J}^*)^{-1} (\vec{x} - \vec{x}_I) \quad (41)$$

The regularization parameter β of LME shape functions may be controlled by adjusting a dimensionless parameter, $\gamma = \beta h^2$ [9], where h is defined as a measure of the nodal spacing. Since N_I is defined in the entire domain, in practice, the function $\exp(-\beta \vec{r})$ truncated by a given tolerance, 10^{-6} , for example, would ensure a reasonable range of neighbours, see [9] for details. This tolerance defines the limit values of the influence radius and is used thereafter to find the neighbour nodes of a given integration point. An additional remark is that in similarity to alternative non-polynomial meshfree basis functions, the LME approximation scheme requires more than $d+1$ nodes to determine the values of the shape functions as well as their derivatives at any point in the convex hull of the nodal set, where d is the dimension of the problem.

This interpolation technique avoids one important shortcoming when using GIMP or B-Spline MPM regarding the computational domain boundaries Steffen *et al.* (2008)[26]. Which is the additional considerations in the applications of the boundary conditions. This is motivated because of their increased extents, it is possible for particles to influence, and be influenced by, nodes that lie outside of the simulation domain. Some researchers have solved this problem with “extra”, or the called “ghost” nodes by other investigators. Anyway this nodes requires especial treatments similar to those employed in the Smoothed Particle Hydrodynamics (SPH), for further details see Liu & Liu (2003)[27]. The approach here described does not require the employ of this artifacts. Due to the fem-compatibility, the LME shape function is degenerated to linear finite element shape function if $d+1$ neighbouring nodes are chosen as the support. Furthermore, with a conveniently adopted *regularization* parameter it is possible to get a GIMP-like shape function. A proof of this statements is observed in figure 5. In this research and in [9], γ is a scalar as the influence area of the shape function is controlled by the Euclidean norm, therefore the search area is geometrically a circle in 2D, or a sphere in 3D. Building upon the idea of anisotropic shape functions, [28] introduced an enhanced version of the original LME scheme, which uses an anisotropic support to deal with tensile instability. Nonetheless this is out of the scope of the present document but will be incorporated in future research.

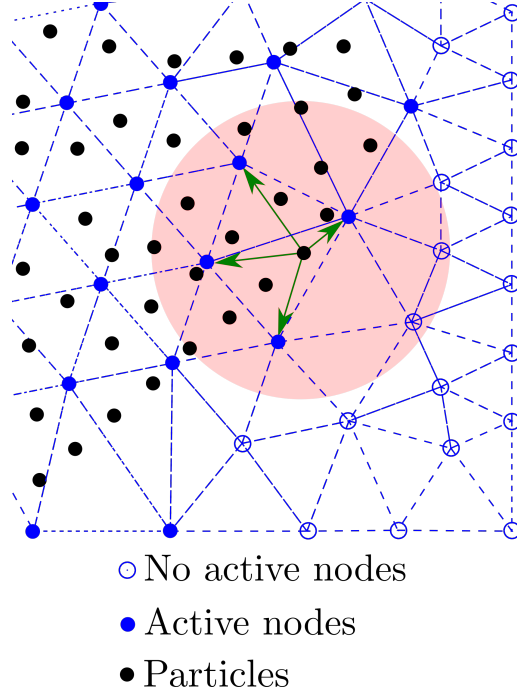


Figure 4: This tolerance defines the limit values of the influence radius and is used thereafter to find the neighbour nodes of a given integration point. The picture also shows the neighbourhood criterion to select those node inside of Ω .

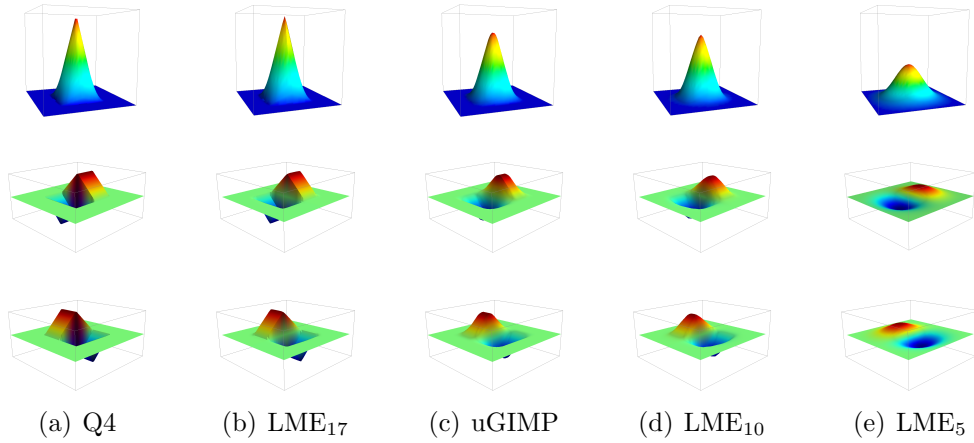


Figure 5: Comparative of linear piecewise shape functions (Q4) and uGIMP shape functions *versus* LME approximation for a two-dimensional arrangement of nodes, and spatial derivatives for several values of $\gamma = \beta/h^2$.

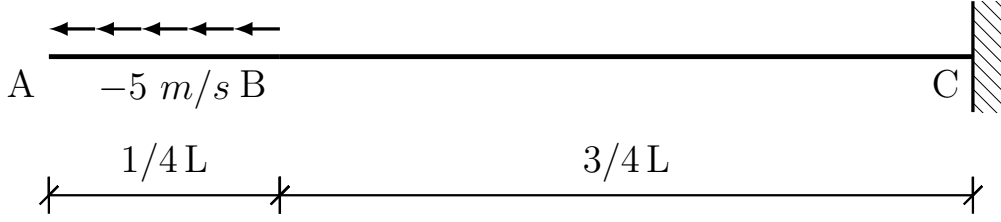


Figure 6: Geometrical description of the Dyka [29] bar.

3. Application to linear elasticity dynamic problems.

This section is devoted to test the ability of both predictor-corrector time integration scheme and the local *max-ent* approximants to overcome spurious oscillations due to the grid crossing and high frequency loads under the context of MPM. Two different test has been adopted for this purpose, the benchmark proposed by Dyka & Ingel (1995)[29] and the test proposed in the PhD thesis of Andersen (2009)[18]. Thought them, the accuracy of the NPC scheme is compared to the standard FE. In addition LME solutions are compared with those provided by Uniform GIMP (uGIMP) and Q4 shape functions. To avoid some mesh-dependent issues, in all calculations a regular background mesh was setted. All simulations were performed with in-house software.

3.1. Dyka bar [29]

This benchmark was proposed due to its ability to shows the capability of the proposed time integration algorithm to avoid velocity fields instabilities. It consists in a one-dimensional bar with a length of 0.1333 meters, sketched in the figure 6. The boundary conditions are: in the right border displacement are constrained ($v|_{x=L} = 0$) and in the left displacement are let free ($\sigma|_{x=0} = 0$). And a initial velocity of $v_o = -5 \text{ m/s}$ is given to the last quarter of it. Finally, the elastic parameters consider for this test are:

- Density : 7833 kg/m^3
- Poisson ratio : 0
- Elastic modulus : $200 \cdot 10^9 \text{ Pa}$

In this case a duration of 0.0001 seconds for the simulation is consider. Therefore, the elastic wave generated travel thorough the bar (from A to C and back to A) at least two times. For the spatial discretization we adopt a set of seven nodal mesh sizes (0.1, 0.3325, 0.5, 1.0, 3.3325, 6.665, 10.0) in millimeters. For each element a number of four particles was selected. In the

initial layout, particles are occupying the exact quadrature points of a linear quadrilateral. With the exception of the uGIMP simulation where gaps or overlap between voxels of each particle are not allowed. In those cases, each particles occupy the center of each cell quarter. For all simulations, time step is controlled by a Courant-Friedrichs-Levy condition of 0.1, where the adopted celerity is computed as,

$$Cel = \max\{\max_{p \in \Omega_p}\{v_p\}, \max_{p \in \Omega_p}\{\sqrt{\frac{E_p}{\rho_p}}\}\} \quad (42)$$

A important consideration regarding modellization concerns to the background mesh. Notice that free border of the bar has a maximum horizontal displacement of 0.03 millimeters, therefore a computational domain with an extra gap of 0.03 millimeters is required in order to accommodate the unconstrained displacement of the particles in the left border of the bar. Naturally this problem arise when the mesh size is small enough that relative displacement of the particles are larger then the distance to the border, so grid crossing phenomena could appear even in those cases with infinitesimal displacements. In this case, an analytical solution is possible thought the characteristics method described in the appendix Appendix A. To measure the convergence of the solutions for the different time integration and approximation schemes the root-mean-square (RMS) error in the velocity field is computed. RMS error is defined as

$$RMS = \sqrt{\frac{1}{N} \sum_p^N (v_p - \hat{v}_p)^2}, \quad (43)$$

225 where v_p and \hat{v}_p are respectively the analytical and numerical solutions evaluated in the final time step in the position of each particle. A first comparative between both time integration scheme is plotted in figure 8. It demonstrates the superior performance of the NPC *versus* the FE. In the NPC the spurious oscillations are quickly mitigated in the first time steps, and does not
230 propagate the error in time in opposite to FE where the simulation becomes unstable after $6E^5$ seconds. Figure 7 also remarks the remarkable difference between both schemes. Figure (9) shows the sensibility of the LME approximation scheme to variations in the a-dimensional parameter β that controls the value of the regularization parameter γ depending of the mesh
235 size. Notice how lower values of gamma exhibits a behaviour with a soft decay in some parts of the simulation due to the increase of nodes adopted to regularize the solutions. This capability could be useful in simulations where extremely noise oscillations could damage the solutions like memory

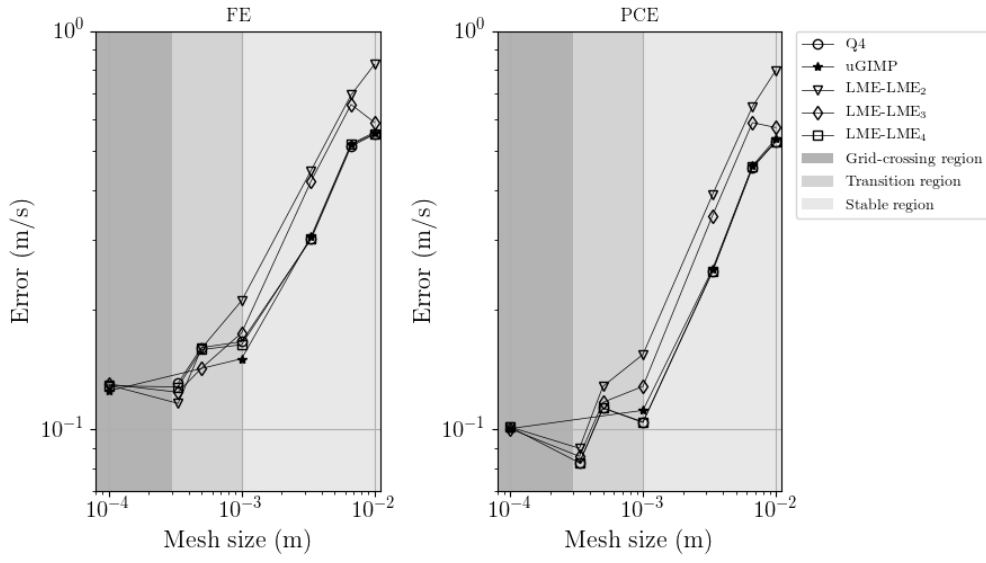


Figure 7: Velocity evolution at the point in the Dyka bar left side, convergence plots for FE and NPC. The plot is subdivided with colours, the darker part of the diagram shows coincides when the relative movement of the particles is large enough to produce the grid crossing phenomena. The lightest part of the diagram coincides when the relative movement of the particles in negligible in comparison with the mesh size. And in the middle region a transition behaviour take place.

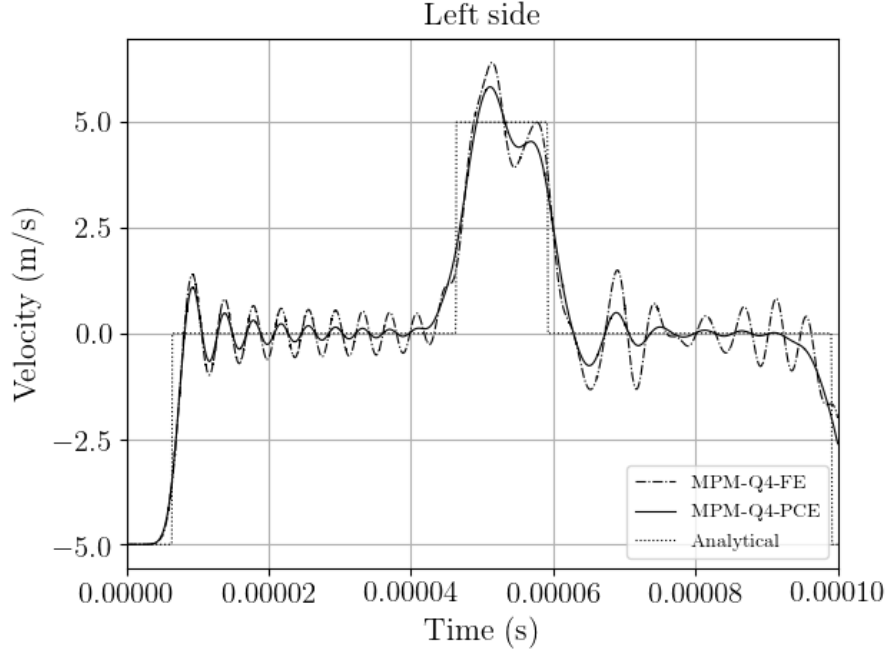


Figure 8: Comparative of the NPC *versus* the FE. In the picture the velocity evolution at the point in the bar left side is plotted.

materials. On the other hand larger values of the parameter β makes the
 240 solution tend to the linear FEM solution as the athermal limit is reached
 [9]. Intermediate values of the regularization parameters give us a compro-
 mise between the both scenarios here described. An additional observation
 concerning the solution sensibility to regularization parameters occurs when
 mesh size decreases. For larger mesh size where the relative particle displace-
 245 ment is negligible in comparison with the cell size, the global behaviour is
 FEM-like, therefore larger values of γ has offers better results. On the other
 hand, when mesh size is small enough to produce grid-crossing and mesh-free
 behaviour is required to ensures the convergence of the solution, tiny values
 of γ has a better performance. Convergence plot in figure (7) shows how
 250 the slope for the larger values of γ decreases monotonically with the value of
 the mesh size, in contrast to larger values of it, whose suffers a punishment
 of the performance when significant movement of the particles occurs as far
 mesh size is reduced. Figure 10 compares the performance of the uGIMP [3]
 shape function *versus* the LME approximation scheme with a adimensional
 255 regularization parameter γ of 4.0. Although it does not shows remarkable
 differences, LME approximats exhibits a more robust behaviour than the
 uGIMP shape functions. Regarding this, notice the absence of uGIMP val-

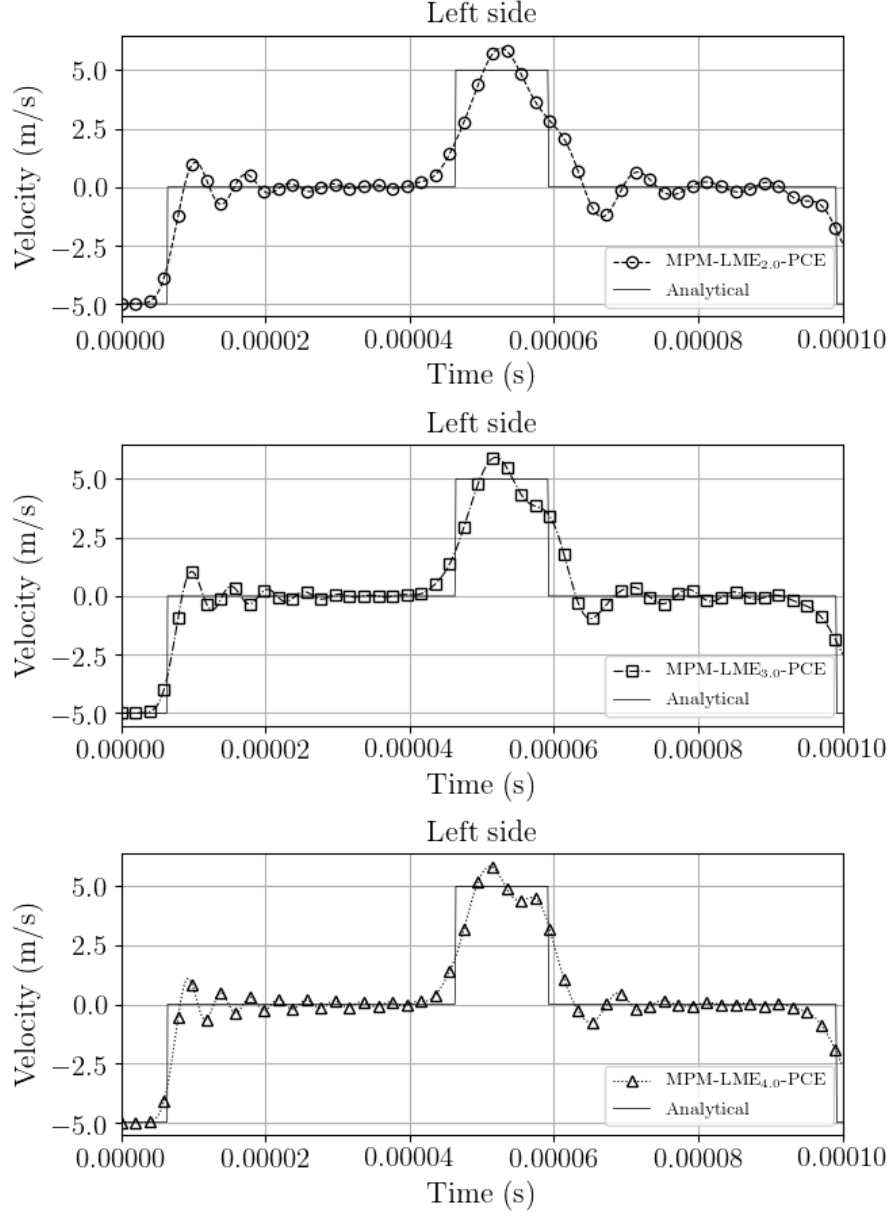


Figure 9: Sensitive of LME approximants performance to changes in the adimensional regularization parameter $\gamma = \beta/h^2$. To illustrate it, the velocity evolution at the point in the bar left side is plotted.

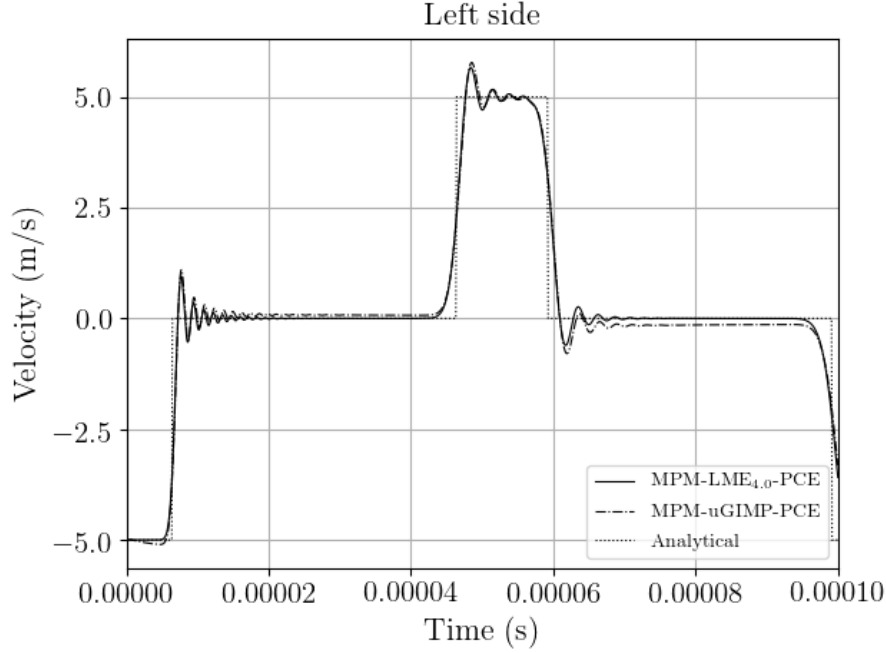


Figure 10: Velocity evolution at the point in the bar left side.

ues for a mesh size of 0.3325 and 0.5 millimeters. This is because during these simulation the uGIMP suffered an unstable increase of the error which
 260 yield unacceptable results. A feasible explanation for this phenomena could be the presence of numerical cancellation which could produce gaps between voxels. Further research should be done in this direction for getting a better comprehension of this phenomena. In opposite, LME approximation does not suffers this phenomena either with irregular nodal layout. Finally, figure 11 compares the solution obtained with OTM [30] *versus* the solution
 265 obtained with MPM, both with same time integration scheme and spatial discretization. For this case the performance of MPM is robust and stable than OTM. During the first half of the simulation both method seem to perform in a similar way, but during the second half of the simulation after the elastic wave has travel from the free border to the fixed one and back, in
 270 OTM the solution becomes noisy than the one performed by MPM.

3.2. Andersen block

The following test was proposed to measure proof the ability of this interpolation technique to deal with grid crossing instabilities. It consists in
 275 the simulation of a square block of soil incrementally loaded by a body force. Details of the problem are sketched in figure 3.2 This test was taken from

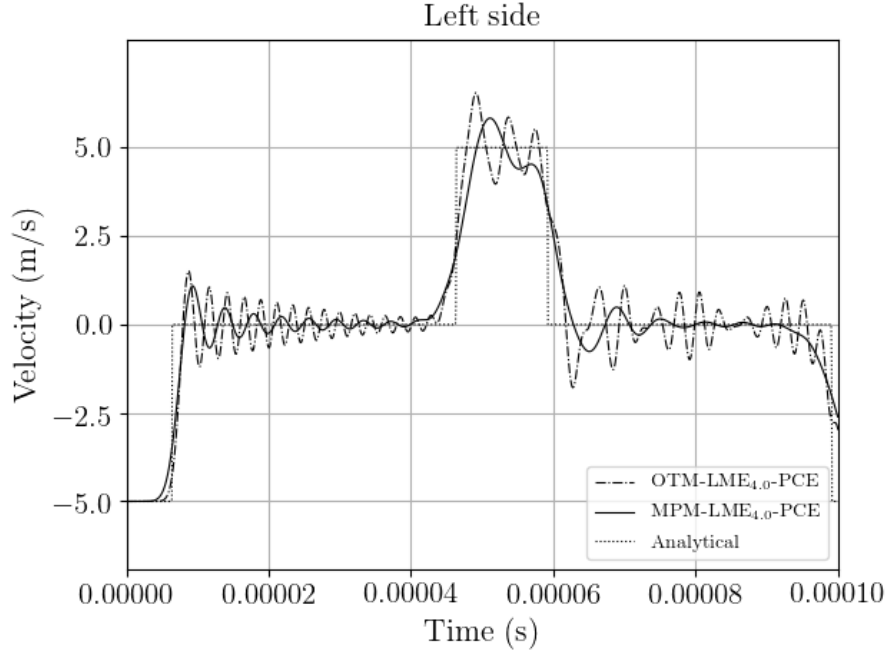


Figure 11: Velocity evolution at the point in the bar left side.

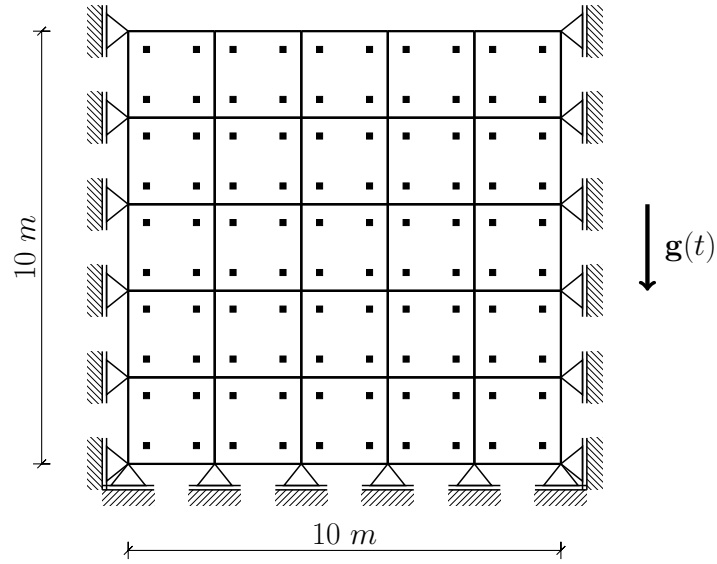


Figure 12: Geometrical description of a soil block

PhD thesis of Andersen (2009)[18]. The elastic parameters consider for this test are:

- Initial density : $6 \cdot 10^3 \text{ kg/m}^3$
- Poisson ratio : 0
- Elastic modulus : 5 MPa

The gravity force is applied as an external force according to the equations (10), (15). Using a total time period of T (20 seconds) to apply the gravity, it is increased from 0 to 9.81 m/s with a sinus function until $T/2$ and then maintained constant until T in order to arrive to a state of equilibrium,

$$\mathbf{g}(t) = \begin{cases} 0.5\mathbf{g}(\sin(\frac{2t\pi}{T} - \frac{\pi}{2}) + 1) & \text{if } t \leq T/2 \\ \mathbf{g} & \text{if } t > T/2 \end{cases} \quad (44)$$

In order to get a stable solution, time step was conducted by a Courant number of 0.1. On the other hand, the explicit predictor-corrector scheme is here employed looking forward getting better results. For the initial spatial discretization four particles per cell ($\Delta x = 2 \text{ m}$) were adopted. The initial layout of particles inside of the cell changes according to the approximation technique adopted. For the bi-linear shape functions and the LME approx-
 imants, the initial position corresponds to the location of the gauss-points in a standard quadratic finite element. For the uGIMP shape function the initial position of each particle is located in the center of each voxel, due to the fact that in the initial situation, the voxel domain should not overlap each others.

Figure 13 shows the evolution of the vertical stress during the loading process. The result is physically realistic as stress increments linearly from the top to the bottom of the specimen, and the value of the vertical stress in a material point located in the bottom of the specimen oscillates centered in 5.2 MPa , which is the analytic value given by $\sigma_{yy} = \rho g h_y$. Figure 14 shows the vertical displacement evolution of a point in the free surface of the block. This figure shows how simulations performed with a bi-linear interpolation technique (Q4) turns out to be unstable during cell-crossing and consequently fails. The uGIMP simulation is more stable than the one performed by the Q4. Despite this is still unstable and could trigger severe oscillations in simulation with non-linear materials. The LME simulation was performed using two kinds of shape functions, one with a low value of the dimensionless parameter, $\gamma = 0.8$, and other with a larger value of it, $\gamma = 3.0$. Notice that the results are both stable, but the larger values of γ give us a very stable solution. This is due to the fact that with larger

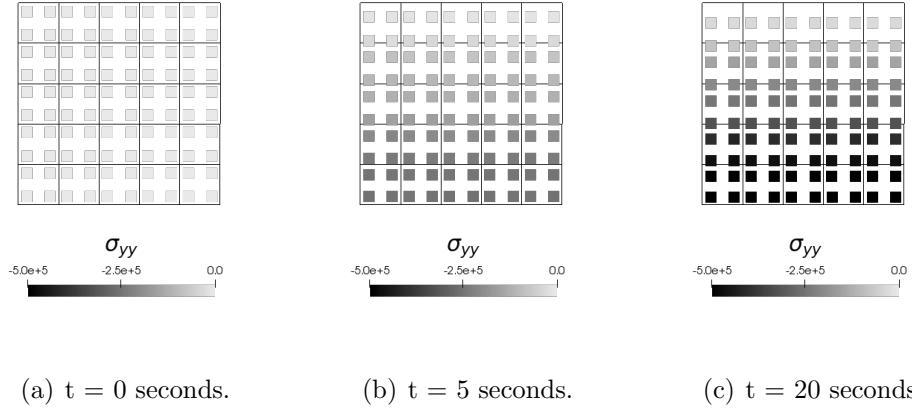


Figure 13: Vertical normal stress and position of material points during the loading process for a soft soil ($E = 5 \text{ MPa}$, $\rho_0 = 6 \cdot 10^3 \text{ kg/m}^3$). Numerical parameters considered for the simulation are : Local *max-ent* shape function $\gamma = 3$ and explicit PC scheme with CFL 0.1.

value of γ , the shape functions behaves in a similar way to the FEM, which performs very accurate in those cases with a reasonable mesh distortion, and with a lower value it behaves in a similar way to the uGIMP. This behaviour was noticed previously by [9], where authors highlight how by adjusting the spatial variation of $\beta(x)$, it is possible to select regions of the domain of analysis which are treated by finite elements and regions that are treated in the style of meshfree methods, with seamless transitions between those regions.

4. Conclusions

We have developed a novel time integration scheme for MPM, and proved how local *max-ent* approximation scheme could be employed as a useful technique in MPM. The NPC arise as a highly efficient alternative for challenging dynamic problems like coupled $u - p_w$ without appeal to expensive implicit time integration algorithms. Also the procedure employed to design the NPC algorithm open the door to revisit a huge variety of time integration schemes developed originally for FEM, which can be rearranged to MPM framework with some modifications. Anyway, further research should be done to improve the formal comprehension of the algorithm good performance. This paper also enhances the suitability of the LME approximation as a general promising alternative to the wide range of approximation techniques developed for the MPM to overcome grid crossing limitations and to avoid the constriction of the uGIMP of a regular mesh or a high density of

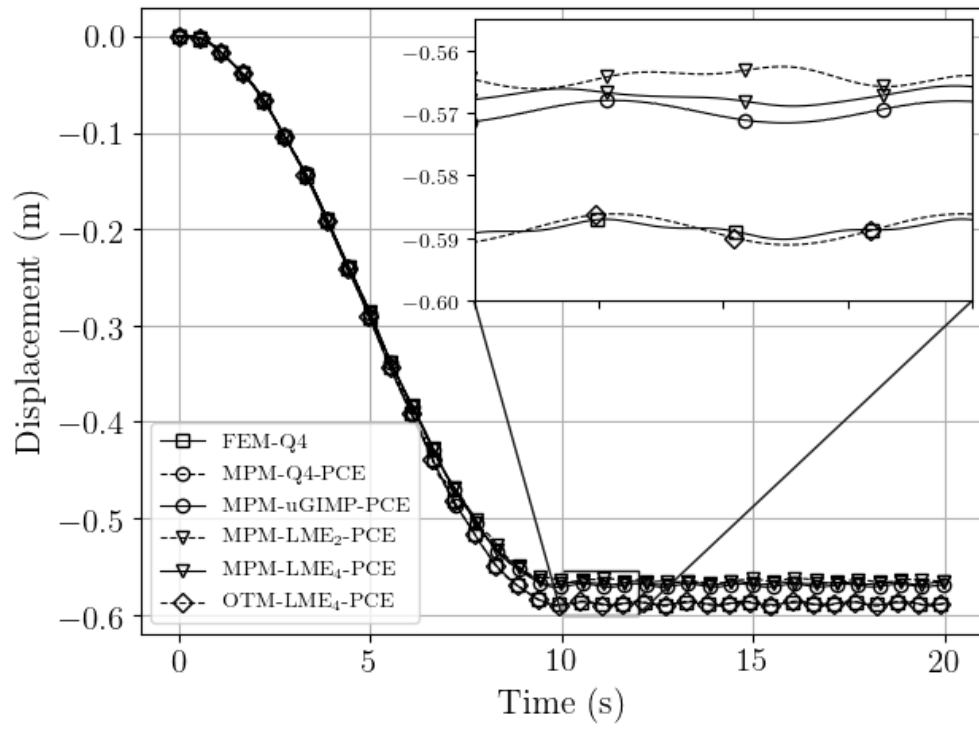


Figure 14: Comparative of the vertical displacement evolution in a point located in the free surface employing different interpolation schemes and numerical techniques.

330 particles per cell. Future research of the group will be on the employ of this
 scheme to improve the localization capabilities of MPM for viscoplastic ma-
 terials. Finally we remark on the possibility of adapting the function $\beta(x)$
 as a second order tensor with the aim of adapt the shape function with the
 strain field which improves the performance of it in the aforementioned local-
 335 ization capabilities. Other possibility is to adapt the value of β to solve the
 equations FEM-like of meshfree-like depending of how behaves the region,
 this could be extremely useful in simulating all together initialization and
 propagation of fast landslides.

If you'd like to thank anyone, place your comments here and remove the
 340 percent signs.

Conflict of interest

The authors declare that they have no conflict of interest.

Glossary

- Γ_d Essential or Dirichlet boundary conditions over $\partial\Omega$. 6, 11
- 345 Γ_n Natural or Nemann boundary conditions over $\partial\Omega$. 6
- β Regularization or thermalization parameter of the LME_β Pareto set. 4
- $\partial\Omega$ Boundary of the continuum domain Ω . Also defined as Γ . 5
- σ Second order tensor which means the Cauchy stress tensor. 6
- ε Second order tensor which means the Cauchy strain tensor. 6
- 350 Ω Continuum domain. 5–7, 17
- u First order tensor which describes the displacement field. 5, 6

Acronyms

- CTLS** Conservative Taylor Least Squares. 3
- DDMP** Dual Domain Material Point. 3
- 355 **FE** Forward Euler. 18–21
- FEM** Finite Element Method. 2, 3, 5, 7, 11, 12, 21, 26, 28

- FLIP** Fluid Implicit Particle. 3
- GIMP** Generalized Interpolation Material Point. 3, 16
- iGIMP** Implicit GIMP. 4
- ³⁶⁰ **LME** Local Maximum-Entropy. 2–4, 12, 15, 16, 18, 19, 21, 23, 25, 26
- MPM** Material Point Method. 2–5, 7, 9–12, 16, 18, 23, 26, 28
- NPC** Newmark Predictor-Corrector. 10, 18–21, 26
- OTM** Optimal Transportation Meshfree. 4, 23
- SPH** Smoothed Particle Hydrodynamics. 16
- ³⁶⁵ **uGIMP** Uniform GIMP. 18, 19, 21, 23, 25, 26

Appendix A. The analytical solution of the 1D Dyka benchmark

For the derivation of this analytical solution we will considered the dynamic behaviour of a 1D elastic bar. The governing equations are the following: (i) The balance of linear momentum,

$$\rho \frac{\partial v}{\partial t} = \frac{\partial \sigma}{\partial x}, \quad (\text{A.1})$$

where σ is the stress value, ρ is the density, and v is the velocity. (ii) The constitutive model, which for convenience of the following developments will be written in terms of displacement and velocities as,

$$\frac{\partial \sigma}{\partial t} = E \frac{\partial \varepsilon}{\partial t}, \quad (\text{A.2})$$

where E is the elastic modulus. (iii) The compatibility equation also in terms of the velocity field,

$$\frac{\partial \varepsilon}{\partial t} = \frac{\partial v}{\partial x}. \quad (\text{A.3})$$

Next for simplicity, we will introduce (A.3) in (A.2), so we get the following system of equations,

$$\frac{\partial v}{\partial t} = \frac{1}{\rho} \frac{\partial \sigma}{\partial x}, \quad (\text{A.4})$$

$$\frac{\partial \sigma}{\partial t} = E \frac{\partial v}{\partial x}. \quad (\text{A.5})$$

Introducing (A.5) in (A.4) and expressing the remaining equation in terms of the displacement, we reach the 1D wave equation for linear elastic materials,

$$\frac{\partial^2 u}{\partial t^2} = \frac{E}{\rho} \frac{\partial^2 u}{\partial x^2} = c^2 \frac{\partial^2 u}{\partial x^2} \quad (\text{A.6})$$

where we have introduced the wave celerity c as,

$$c = \sqrt{\frac{E}{\rho}} \quad (\text{A.7})$$

Alternative, rearranging both equations (A.4) and (A.5) it is possible to join them in a single system of equations as,

$$\frac{\partial}{\partial t} \begin{bmatrix} \sigma \\ v \end{bmatrix} + \begin{bmatrix} 0 & -E \\ -1/\rho & 0 \end{bmatrix} \begin{bmatrix} \frac{\partial \sigma}{\partial x} \\ \frac{\partial v}{\partial x} \end{bmatrix} = \mathbf{0}. \quad (\text{A.8})$$

This expression can be written in a more compact format as,

$$\frac{\partial \phi}{\partial t} + \mathbf{A} \frac{\partial \phi}{\partial x} = \mathbf{0} \quad (\text{A.9})$$

where both variables are joined in a single vectorial variable ϕ and \mathbf{A} in coupling matrix between both equations,

$$\phi = \begin{bmatrix} \sigma \\ v \end{bmatrix}, \quad \mathbf{A} = \begin{bmatrix} 0 & -E \\ -1/\rho & 0 \end{bmatrix}.$$

Note that the nature of is still hyperbolic despite the fact it does not have a second order temporal derivative as (A.6). A proof of this can be easily obtained if we get the zeros of the hypersurface defined by (A.6). And later the eigenvalues of \mathbf{A} in (A.9). In both cases, eigenvalues are real and distinct
370
 $(\lambda = \pm \sqrt{\frac{E}{\rho}})$, therefore the system is called strictly hyperbolic.

For a more general description in the following, we will assume that \mathbf{A} has n different eigenvalues $\{\lambda_1, \lambda_2, \dots, \lambda_i, \dots, \lambda_n\}$ and n eigenvectors $\{\vec{x}^1, \vec{x}^2, \dots, \vec{x}^i, \dots, \vec{x}^n\}$

satisfying that $\mathbf{A}\vec{x} = \lambda\vec{x}$. Now we introduce the matrix \mathbf{P} whose columns are the n eigenvalues \mathbf{x}

$$\mathbf{P} = \{\vec{x}^1, \vec{x}^2, \vec{x}^3, \dots, \vec{x}^n\}. \quad (\text{A.10})$$

Diagonalizing \mathbf{A} using \mathbf{P} we get

$$\Lambda = \mathbf{P}^{-1} \mathbf{A} \mathbf{P}, \quad (\text{A.11})$$

where $\Lambda_{ii} = \lambda_i$. Next we will define a vector \mathfrak{R} such that:

$$\phi = \mathbf{P} \mathfrak{R} \quad (\text{A.12})$$

we will assume to be integrable. Expanding the above expression with the chain rule and passing the matrix \mathbf{P} to left hand side of the equality we get,

$$d\vec{\mathfrak{R}} = \frac{\partial \mathfrak{R}}{\partial t} dt + \frac{\partial \mathfrak{R}}{\partial x} dx = \mathbf{P}^{-1} \left(\frac{\partial \phi}{\partial t} dt + \frac{\partial \phi}{\partial x} dx \right) \quad (\text{A.13})$$

and setting the terms we get,

$$\frac{\partial \mathfrak{R}}{\partial t} = \mathbf{P}^{-1} \frac{\partial \phi}{\partial t}, \quad \frac{\partial \mathfrak{R}}{\partial x} = \mathbf{P}^{-1} \frac{\partial \phi}{\partial x} \quad (\text{A.14})$$

Next, if we multiply (A.9) by \mathbf{P}^{-1} we get:

$$\mathbf{P}^{-1} \frac{\partial \phi}{\partial t} + (\mathbf{P}^{-1} \mathbf{A} \mathbf{P}) \mathbf{P}^{-1} \frac{\partial \phi}{\partial x} = \mathbf{0} \quad (\text{A.15})$$

finally introducing the expressions (A.14) we reach to

$$\frac{\partial \mathfrak{R}}{\partial t} + \Lambda \frac{\partial \mathfrak{R}}{\partial x} = \mathbf{0} \quad (\text{A.16})$$

which consists of n uncoupled equations as Λ is diagonal matrix as we can see in (A.11). Each of this equations are 1D scalar convective transport equations, with solutions of the form:

$$\mathfrak{R}^{(i)} = F^{(i)}(x - \lambda^{(i)}t) \quad (\text{A.17})$$

This uncoupled system, has, therefore, a set of n characteristics. These magnitudes \mathfrak{R}_i which propagate along characteristics are known as ‘‘Riemann invariants’’ of the problem. Here we have a 1D configuration, so the domain is $\Omega : (0, L) \times (0, T)$. For the closure of the problem we require:

- “n” initial conditions of the form $\mathfrak{R}_i(x, t = 0) = h_i(x)$, where $i = 0, \dots, n$, and $h_i(x)$ is a vectorial function given by the physical variables of the problem.
- “n” boundary conditions.

Now particularizing the previous equations for the 1D elastic bar described in [29], we get that the matrix \mathbf{P} is the following:

$$\mathbf{P} = \begin{bmatrix} -\sqrt{E\rho} & \sqrt{E\rho} \\ 1 & 1 \end{bmatrix}$$

and its inverse is:

$$\mathbf{P}^{-1} = \frac{1}{2\sqrt{E\rho}} \begin{bmatrix} -1 & \frac{1}{\sqrt{E\rho}} \\ 1 & \frac{1}{\sqrt{E\rho}} \end{bmatrix}$$

And introducing the value of the inverse matrix \mathbf{P}^1 in the Riemann definition (A.12) we get the following system of equations,

$$\mathfrak{R}^I = \frac{1}{2\sqrt{\rho E}} \left(-\sigma + v \sqrt{\rho E} \right) \quad (\text{A.18})$$

$$\mathfrak{R}^{II} = \frac{1}{2\sqrt{\rho E}} \left(\sigma + v \sqrt{\rho E} \right) \quad (\text{A.19})$$

From (A.18) and (A.19) we can obtain the values of the stress and the velocity as:

$$v = \mathfrak{R}^I + \mathfrak{R}^{II} \quad , \quad \sigma = \sqrt{E\rho} (\mathfrak{R}^{II} - \mathfrak{R}^I) \quad (\text{A.20})$$

The boundary conditions are in both cases of radiation as there is not wave in-going from the exterior. So for the right side (fixed boundary) we get the following conditions:

$$\mathfrak{R}^{II} = 0 \quad \text{and} \quad v_{x=L} = 0$$

Therefore $\sigma_{x=L} = -2\sqrt{\rho E} \mathfrak{R}^I$. And in the left side (free boundary) we get the following conditions:

$$\mathfrak{R}^I = 0 \quad \text{and} \quad \sigma_{x=0} = 0$$

380 Therefore $v_{x=0} = 2\mathfrak{R}^{II}$. Finally, applying this conditions in the elastic bar sketched in figure 6, is possible to obtain the velocity history in the right side of the bar plotted in the figure A.15 and the stress in the last quarter side of the Dyka bar plotted in the figure A.16 as is demanded in [29].

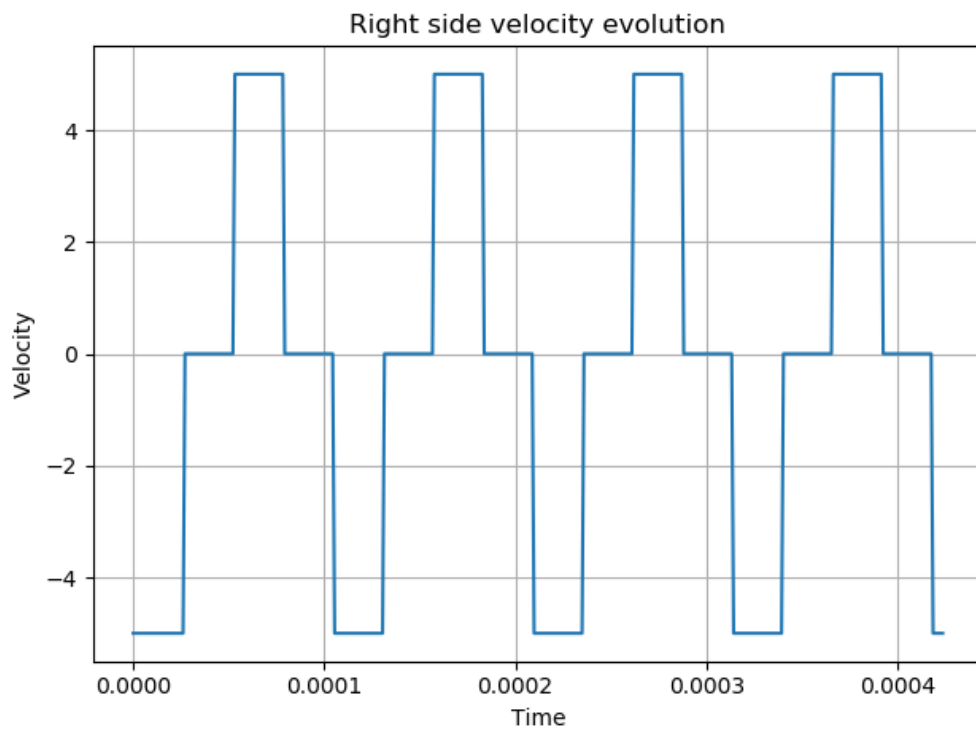


Figure A.15: Analytical solution for the velocity in the right side of the Dyka bar.

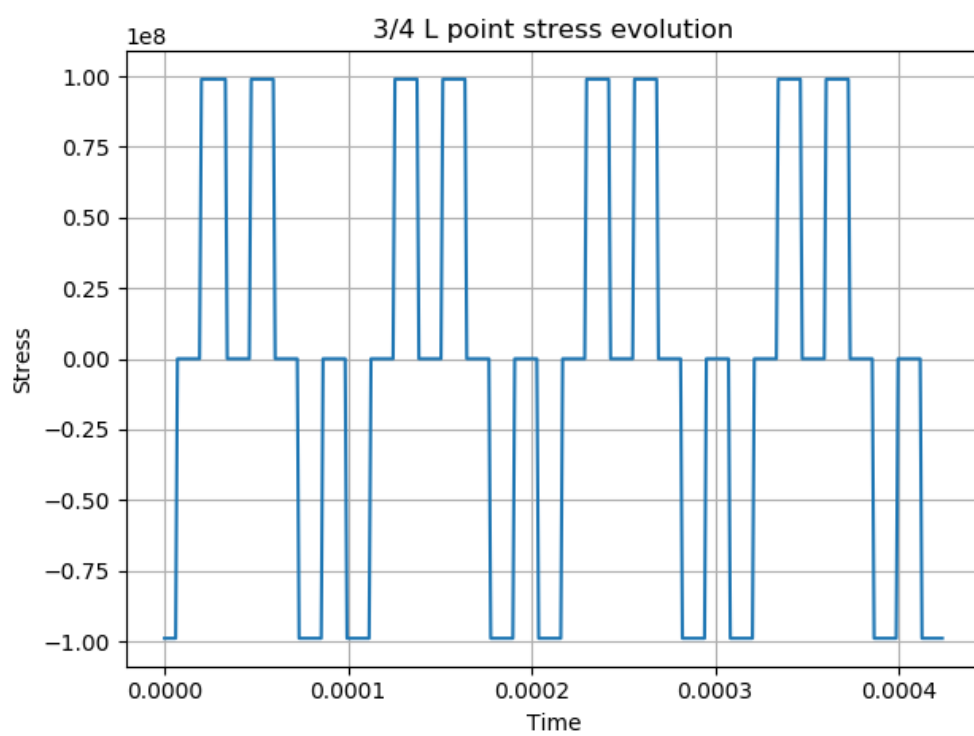


Figure A.16: Analytical solution for the stress in the last quarter of the Dyka bar.

References

- 385 [1] D. L. Sulsky, H. Schreyer, Z. Chen, A particle method for history-dependent materials, *Computer Methods in Applied Mechanics and Engineering* 118 (1) (1994) 179–196. doi:10.1016/0045-7825(94)90112-0.
- 390 [2] J. U. Brackbill, H. M. Ruppel, FLIP: A method for adaptively zoned, particle-in-cell calculations of fluid flows in two dimensions, *Journal of Computational Physics* doi:10.1016/0021-9991(86)90211-1.
- [3] S. G. S. G. Bardenhagen, E. M. Kober, The generalized interpolation material point method, *CMES - Computer Modeling in Engineering and Sciences* 5 (6) (2004) 477–495.
- 395 [4] M. Steffen, R. M. Kirby, M. Berzins, Analysis and reduction of quadrature errors in the material point method (MPM), *International Journal for Numerical Methods in Engineering* 76 (6) (2008) 922–948. doi:10.1002/nme.2360.
URL <http://doi.wiley.com/10.1002/nme.2360>
- 400 [5] D. Z. Zhang, X. Ma, P. T. Giguere, Material point method enhanced by modified gradient of shape function, *Journal of Computational Physics* 230 (16) (2011) 6379–6398. doi:10.1016/J.JCP.2011.04.032.
URL <https://www.sciencedirect.com/science/article/pii/S0021999111002804>
- 405 [6] T. R. Dhakal, D. Z. Zhang, Material point methods applied to one-dimensional shock waves and dual domain material point method with sub-points, *Journal of Computational Physics* 325 (2016) 301 – 313. doi:<https://doi.org/10.1016/j.jcp.2016.08.033>.
URL <http://www.sciencedirect.com/science/article/pii/S0021999116303904>
- 410 [7] R. Tielen, E. Wobbes, M. Mller, L. Beuth, A high order material point method, *Procedia Engineering* 175 (2017) 265 – 272, proceedings of the 1st International Conference on the Material Point Method (MPM 2017). doi:<https://doi.org/10.1016/j.proeng.2017.01.022>.
URL <http://www.sciencedirect.com/science/article/pii/S187770581730022X>
- [8] E. Wobbes, M. Moller, V. Galavi, C. Vuik, M. Möller, V. Galavi, C. Vuik, M. Moller, V. Galavi, C. Vuik, Conservative Taylor Least

- 420 Squares reconstruction with application to material point methods:
Conservative Taylor Least Squares reconstruction, *International Journal for Numerical Methods in Engineering* 117 (3) (2018) 271–290. doi:10.1002/nme.5956.
- 425 [9] M. Arroyo, M. Ortiz, Local maximum-entropy approximation schemes: A seamless bridge between finite elements and meshfree methods, *International Journal for Numerical Methods in Engineering* doi:10.1002/nme.1534.
- 430 [10] P. Navas, S. López-Querol, R. C. Yu, M. Pastor, Optimal transportation meshfree method in geotechnical engineering problems under large deformation regime, *International Journal for Numerical Methods in Engineering* doi:10.1002/nme.5841.
- [11] B. Li, A. Kidane, G. Ravichandran, M. Ortiz, Verification and validation of the Optimal Transportation Meshfree (OTM) simulation of terminal ballistics, *International Journal of Impact Engineering* doi:10.1016/j.ijimpeng.2011.11.003.
- 435 [12] E. Wobbes, R. Tielen, M. Möller, C. Vuik, Comparison and unification of material-point and optimal transportation meshfree methods, *Computational Particle Mechanics* doi:10.1007/s40571-020-00316-7.
- 440 [13] Q. A. Tran, W. Sołowski, Temporal and null-space filter for the material point method, *International Journal for Numerical Methods in Engineering* doi:10.1002/nme.6138.
- [14] T. J. Charlton, W. M. Coombs, C. E. Augarde, iGIMP: An implicit generalised interpolation material point method for large deformations, *Computers & Structures* 190 (2017) 108–125. doi:10.1016/j.compstruc.2017.05.004.
- 445 [15] E. L. Wilson, I. Farhoomand, K. J. Bathe, Nonlinear dynamic analysis of complex structures, *Earthquake Engineering & Structural Dynamics* 1 (3) (1972) 241–252. doi:10.1002/eqe.4290010305. URL <http://doi.wiley.com/10.1002/eqe.4290010305>
- 450 [16] J. Chung, G. M. Hulbert, A Time Integration Algorithm for Structural Dynamics With Improved Numerical Dissipation: The Generalized-alpha Method, *J. Appl. Mech.* 60 (2) (1993) 371. doi:10.1115/1.2900803.

- [17] S. G. S. Bardenhagen, Energy Conservation Error in the Material Point Method for Solid Mechanics, *Journal of Computational Physics* 180 (1) (2002) 383–403. doi:10.1006/JCPH.2002.7103.
- [18] S. M. Andersen, Material-Point Analysis of Large-Strain Problems: modelling of landslides, Ph.D. thesis, Department of Civil Engineering, Aalborg University (2009).
- [19] J. Guilkey, J. A. Weiss, Implicit time integration for the material point method : Quantitative and algorithmic comparisons with the finite element method, *International Journal for Numerical Methods in Engineering*.
- [20] X. Zhang, Z. Chen, Y. Liu, The Material Point Method: A Continuum-Based Particle Method for Extreme Loading Cases, Elsevier, 2016. doi:10.1016/b978-0-12-407716-4.00003-x.
- [21] T. J. R. Hughes, The finite element method : linear static and dynamic finite element analysis, Dover Publications, 2000.
- [22] X. Liu, On the stability of a newmark’s scheme-based predictor-corrector algorithm, *Computers Structures - COMPUT STRUCT* 53 (1994) 27–33. doi:10.1016/0045-7949(94)90126-0.
- [23] O. C. Zienkiewicz, J. Z. Zhu, The superconvergent patch recovery and a posteriori error estimates. part 1: The recovery technique, *International Journal for Numerical Methods in Engineering* 33 (7) (1992) 1331–1364. doi:10.1002/nme.1620330702.
- [24] W. Zdzislaw, The material point method in large strain engineering problems, *Computer Methods in Applied Mechanics and Engineering* 193 (39-41 SPEC. ISS.) (2004) 4417–4438. doi:10.1016/j.cma.2004.01.035.
- [25] E. Jaynes, Information Theory and Statistical Mechanics, *The Physical Review* 106 (4) (1957) 620–630.
- [26] M. Steffen, P. C. Wallstedt, J. Guilkey, R. M. Kirby, M. Berzins, Examination and analysis of implementation choices within the Material Point Method (MPM), *CMES - Computer Modeling in Engineering and Sciences* 31 (2) (2008) 107–127.
- [27] G. R. G.-R. Liu, M. B. Liu, Smoothed particle hydrodynamics : a meshfree particle method, World Scientific, 2003.

URL https://books.google.es/books/about/SmoothedParticleHydrodynamics.html?id={_}cwFMmEQvZQC{&}redir{_-}esc=y

- 490 [28] S. Kumar, K. Danas, D. M. Kochmann, Enhanced local maximum-
entropy approximation for stable meshfree simulations, *Computer Meth-
ods in Applied Mechanics and Engineering* doi:10.1016/j.cma.2018.
10.030.
- 495 [29] C. Dyka, R. Ingel, An approach for tension instability in smoothed par-
ticle hydrodynamics (SPH), *Computers & Structures* 57 (4) (1995) 573–
580. doi:10.1016/0045-7949(95)00059-P.
- [30] B. Li, F. Habbal, M. Ortiz, Optimal transportation meshfree approx-
imation schemes for fluid and plastic flows, *International Journal for
Numerical Methods in Engineering* 83 (12) (2010) 1541–1579. doi:
500 10.1002/nme.2869.
URL <http://doi.wiley.com/10.1002/nme.2869>